

Article

Different Mechanism Effect between Gas-Solid and Liquid-Solid Interface on the Three-Phase Coexistence Hydrate System Dissociation in Seawater: A Molecular Dynamics Simulation Study

Zhixue Sun ^{1,*}, Haoxuan Wang ¹, Jun Yao ¹, Chengwei Yang ², Jianlong Kou ¹, Kelvin Bongole ¹, Ying Xin ¹, Weina Li ¹ and Xuchen Zhu ¹

¹ School of Petroleum Engineering, China University of Petroleum (East China), Qingdao 266580, China; 13506428396@163.com (H.W.); yaojunhdpu@126.com (J.Y.); kjl@zjnu.cn (J.K.); kbongole@yahoo.com (K.B.); 15764220169@163.com (Y.X.); vinacomeonbest@icloud.com (W.L.); 15764265298@163.com (X.Z.)

² Exploration & Development Research Institute, Petro China Changqing Oilfield Company, Xi'an 136201, China; yangcw_cq@petrochina.com.cn

* Correspondence: upcszx@upc.edu.cn; Tel./Fax: +86-186-0546-0123

Received: 22 October 2017; Accepted: 19 December 2017; Published: 21 December 2017

Abstract: Almost 98% of methane hydrate is stored in the seawater environment, the study of microscopic mechanism for methane hydrate dissociation on the sea floor is of great significance to the development of hydrate production, involving a three-phase coexistence system of seawater (3.5% NaCl) + hydrate + methane gas. The molecular dynamics method is used to simulate the hydrate dissociation process. The dissociation of hydrate system depends on diffusion of methane molecules from partially open cages and a layer by layer breakdown of the closed cages. The presence of liquid or gas phases adjacent to the hydrate has an effect on the rate of hydrate dissociation. At the beginning of dissociation process, hydrate layers that are in contact with liquid phase dissociated faster than layers adjacent to the gas phase. As the dissociation continues, the thickness of water film near the hydrate-liquid interface became larger than the hydrate-gas interface giving more resistance to the hydrate dissociation. Dissociation rate of hydrate layers adjacent to gas phase gradually exceeds the dissociation rate of layers adjacent to the liquid phase. The difficulty of methane diffusion in the hydrate-liquid side also brings about change in dissociation rate.

Keywords: methane hydrate; adjacent phase; dissociation rate; molecular dynamic simulation

1. Introduction

Gas hydrates are non-stoichiometric crystalline compounds in which gas molecules reside in polyhedral water cages that are stabilized by hydrogen bonds in low-temperature and high-pressure condition. There are at least three different hydrate structures: sI, sII, and sH, the most common in nature being sI. Methane hydrates are the most widespread type of clathrate thought to exist in nature primarily as type sI in the permafrost and deep ocean regions.

Research on gas hydrates has been motivated to a great extent due to the significant amount of methane in hydrate deposits. The availability of methane in hydrates makes hydrates a key future energetic resource, whose exploitation represents a technical challenge. Studies that were conducted earlier by other researchers aimed in establishing efficient ways for exploration of gas hydrates [1–4] with a broad range of laboratory experiments [5–14] and field scale simulations [15–18]. However, the microscopic mechanism study of hydrate dissociation and its production process faces a great limitation with the available conventional methods. It defers the development of gas hydrate

exploitation. Molecular dynamics simulation is an effective way to study the microscopic mechanism of hydrate previously and most used by researchers.

Molecular dynamics simulations (MD) is a powerful tool to study the microscopic structures and dynamics in condensed phases with little time resolutions, and yields a significant value of information, such as thermodynamic and equilibrium properties [19–25], thermal conductivity [26–29], nucleation [30–34], and growth [35–39] of hydrates. Dissociation mechanism of hydrates has also been a focus of MD simulation; many authors studied the dissociation of both spherical methane hydrate nanoclusters and planar systems. Báez and Clancy [40] performed MD simulations of dissolution of fully-occupied spherical hydrate clusters containing about 245 and 400 water molecules in surrounding liquid phases composed of melted hydrate and pure water. They found that dissociation was essentially stochastic, taking place more in a stepwise fashion. Tse and Klug [41] showed that the hydrate self-preservation effect could delay the kinetics of hydrate decomposition by the formation of an ice layer on the surface of a decomposed hydrate. Takeya et al. [42,43] also studied the anomalous preservation of methane hydrate and think that methane hydrate that is stabilized by its self-preservation phenomenon might one of the most favorable and environmentally friendly candidates for methane storage. English et al. [44–46] studied the dissociation of methane hydrate by both perturbations with electromagnetic fields [42] and conventional heating [45,46]. They showed the diffusion of methane from hydrate into adjacent phases is another important step, which influences the overall break-up rate. Myshakin et al. [47] carried out MD simulations of the dissociation of methane hydrate with 85%, 95%, and 100% overall occupancy in contact with pure water. They showed the tendency of dissociation rate, which displays an Arrhenius temperature dependence. Bagherzadeh et al. [48] performed dissociation of methane hydrate in touch with a silica surface. The hydrate was seen dissociating layer by layer between the silica surfaces. Alavi and Ripmeester [49], and Bagherzadeh et al. [50] studied the heat transfer that is involved in dissociation process. All of the previous studies provide valuable insights into various aspects of hydrates dissociation process. However, many problems have not yet been solved, with different studies often reaching different conclusions.

In the marine environment, regions of hydrate-bearing sediments usually in contact with various phase states like seawater and methane gas. However, in the previous simulation researchers, most of the authors studied the hydrate dissociation behavior only with single adjacent phase. Little research has exploited the dissociation mechanism in a three-phase coexistence system with both adjacent liquid and gas phases. To study the multiple phase combination effects, we build a three-phase coexistence system with liquid water, solid hydrate crystal, and methane gas with 3.5% of NaCl added to the water phase to simulate the average salinity of seawater. Mimachi et al. [51] used phase contrast X-ray computed tomography, cryo-SEM, and powder X-ray diffraction to investigate the stability of methane hydrate with up to a few percent of sodium chloride, and proved that the dissociation rate of methane hydrate containing sodium chloride was faster than that of pure methane hydrate. Xu et al. [52] also showed that the dissociation of methane hydrates with and without electrolytes have a distinct difference from a MD simulation. The presence of electrolytes could promote hydrate dissociation by electrostatic force. The strong electrostatic force from inorganic ions attracts the water molecules to escape from the restraint of hydrogen bonds, and thus can break down the water-cage structure of methane hydrate. Therefore, in the simulation of gas hydrate in marine sediments, adding 3.5% of NaCl is necessary. The addition of 3.5% of NaCl makes the simulation have a closer resemblance to the real environment of gas hydrate in marine sediments. From the dissociation process for the three-phase coexistence hydrate system and the effect of adjacent phases, regions in hydrate slab in contact with multiple phases show a different behavior in the dissociation rate. At the beginning of dissociation process, the hydrate layer in contact with liquid phase dissociated faster than the layer adjacent to the gas phase. However, as the dissociation continues, the phenomenon is reversed. Dissociation rate of hydrate layer adjacent to gas phase gradually exceeds the layer adjacent to the liquid phase.

2. Methods

2.1. Simulation System

There are three phases in the simulation system. The solid phase consists of $2 \times 2 \times 8$ unit cells of structure I crystalline hydrate filled with methane molecules of lattice size of $2.375 \text{ nm} \times 2.375 \text{ nm} \times 9.5 \text{ nm}$. The location of oxygen atoms in the sI hydrate lattice follows the single crystal X-ray analysis [53], and the hydrogen atoms were then added randomly and re-oriented to follow the Bernal-Fowler ice rule. The liquid phase that is in contact with the hydrate slab consists of 532 water molecules, 6 Na ions, and 6 Cl ions to reproduce the 3.5% salinity in the seawater environment. The gas phase in contact with the hydrate slab consists of 336 methane molecules. Simulation boxes of hydrate-water and hydrate-methane are arranged along z-dimension, respectively, such that the interfacial area is in the x-y plane. The total size of simulation cell is $2.375 \text{ nm} \times 2.375 \text{ nm} \times 18.3418 \text{ nm}$. A snapshot of our system shown in Figure 1.

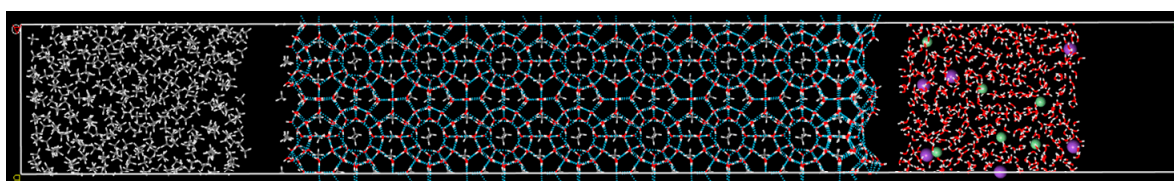


Figure 1. Snapshot of the initial configuration of the three-phase system. H_2O molecules in red and white and CH_4 molecules in white and gray colors. The green and purple dots in the H_2O slab represent Na and Cl ions, respectively. The blue dotted lines in hydrate slab are the hydrogen bond network.

2.2. Simulation Details

MD simulations were carried out with Forcite modules in Materials Studio of Accelrys Inc. The consistent valence force field (CVFF) was used to describe the interactions in the system, earlier used by Greathouse et al. [54], Xu et al. [52], and Wen's group [55,56] to simulate the CH_4 , CO_2 , and H_2 hydrate. Liu et al. [57] showed the ability of the consistent valence force field (CVFF) to reproduce the strengths of intermolecular interactions of all the relevant molecular dimers in methane hydrate from highly accurate CCSD(T)/aug-cc-pVQZ calculations in a satisfactory manner. In their researchers, these authors showed that the CVFF force field provides a greatly qualitative description for gas hydrates. Simple point charge (SPC) water model is used with the on-site charge on "H" and "O" atoms are $+0.41e$ and $-0.82e$, respectively, while the charge on "C" and "H" atoms of CH_4 molecules are $-0.4e$ and $+0.1e$. SPC is the default water model for CVFF in Materials Studio, and can give qualitatively reasonable results in the study of clathrate hydrate [58]. In this work, the author employed both MD simulation with NPT ensemble (isothermal-isobaric ensemble) and the periodic boundary condition at a temperature span of 243 K to 263 K, with the time step set to 1 fs. The pressure of simulation system was controlled by the Berendsen method in 30 MPa. The Nose-hoover method was used to control the system temperature. The Atom-based method was employed for the van der Waals interactions with a 12.5 \AA cutoff distance, while Ewald summation used in calculating the long-range electrostatic interactions.

It should be noted that the melting point of water model has a significant effect on hydrate melting point, which has been proved by several authors [34,59,60]. This effect had already been pointed out by Conde and Vega, who found a correlation between the estimation of hydrate melting point and the estimated melting temperature of Ice Ih for different H_2O models at the same pressure. Sarupria compared the MD simulations result with experimental data, and found that the difference in the melting points ($T_m(\text{hydrate}) - T_m(\text{ice})$) that was obtained from MD simulations is in good agreement with the experimental value. Under the experimental conditions, the hydrate melting point at 30 MPa is 295 K [61], 22 K higher than the melting point of Ice Ih. The melting point of SPC model is 190 K

at 30 MPa, the corresponding hydrate melting point is about 212 K. In our simulation work, the temperature range of 243 K–263 K is higher than the melting point of both Ice Ih and hydrate at 30 MPa.

The total simulation process comprises of three steps: At the beginning, the initial model system was optimized by both steepest descent and conjugate gradient, and then a 100 ps MD simulation was used with immobilized hydrate slab to release the extra tension at the interface between hydrate and adjacent phases. Finally, loosening the hydrate slab and allowing enough time for the simulation to run until the hydrate melts completely.

3. Results and Discussion

3.1. Dissociation Process of Hydrate Slab in Three Phase System

The trajectory during the MD simulation shows clearly the dissociation process of hydrate slab from the three phase system; the methane molecules in the partially filled cages diffuse quickly at the interface region to the liquid or gas phase. As time elapse, the partial cages become distorted because of losing guest molecules, while the closed cages remain intact (Figure 2), this state will continue until the closed cages get enough energy to activate, which depends on the temperature. At sufficient supplied temperature, the closed cages followed by the partially filled cages begin to disintegrate, and the hydrate slab dissociation trend starts from the interfaces towards the center (Figure 3). This disintegration phenomena are the same seen by Báez et al. [40] and English et al. [45]. This phenomena suggest that no matter what phases the hydrate region are in contact in the seawater environment, the dissociation will occur from the outside interfaces to the core of the hydrate.

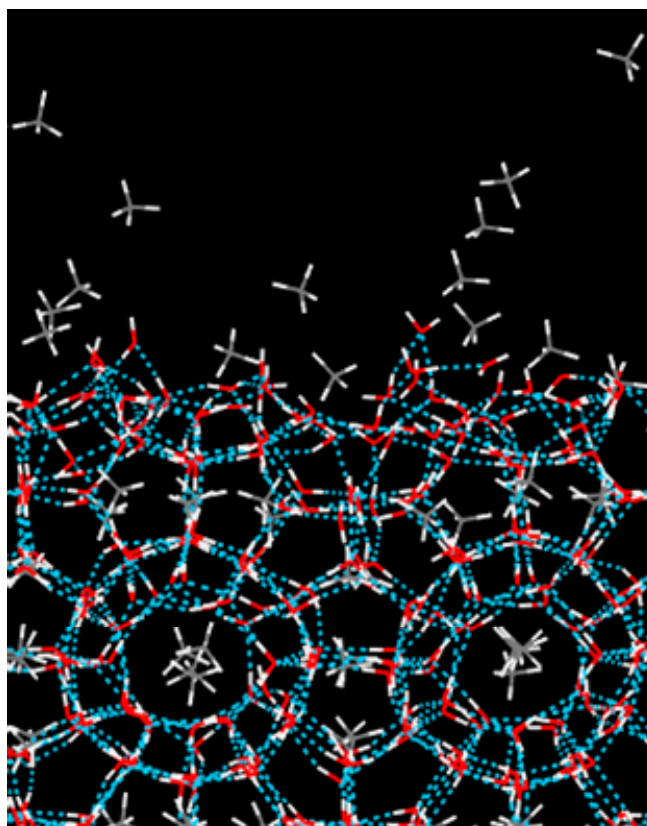


Figure 2. The diffusion of methane molecules from partially filled cages and partial cages distortion.

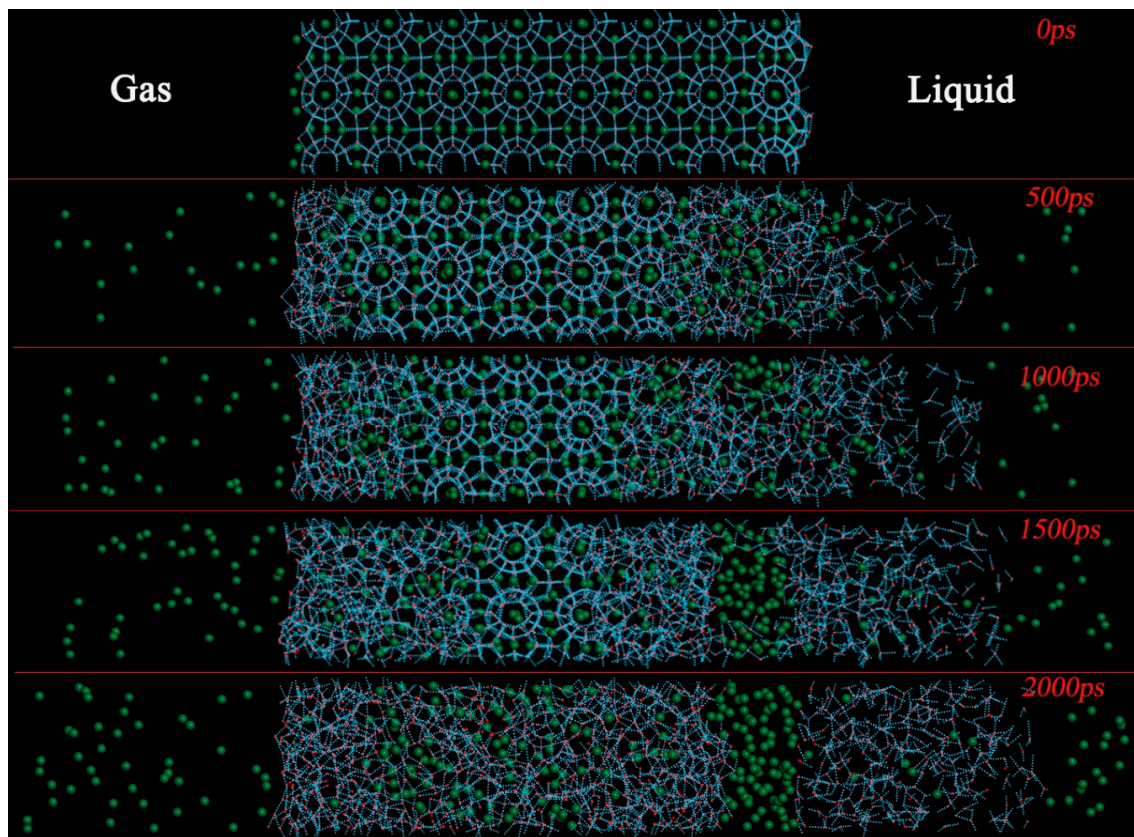


Figure 3. A layer by layer breakdown of closed cages in hydrate slab from the two interfaces to center. To facilitate the observation of hydrate dissociation process, all molecules in liquid and gas phases and H₂O molecules in hydrate slab are hidden. CH₄ molecules in hydrate slab is displayed as green ball, and the blue dotted lines in hydrate slab are hydrogen bond.

3.2. Effect of the Adjacent Phases on Dissociation Process

The hydrate slab has been divided into seven layers that are perpendicular to the Z-direction, so as to study different dissociation behavior for regions of hydrate-bearing sediments in contact with various phases in the seawater environment. The configuration shown in Figure 4 is used to discuss the effect of the two adjacent phase states. Layer A1, A2, and A3 near the liquid phase correspond to the liquid side, while the adjacent three layers near the gas phase correspond to the gas side. Symbol “L” and “G” are used to represent the liquid and gas side, respectively. Although the subsequent decomposition process will weaken the phase difference of the two side, the initial adjacent phase of hydrates will still affect their decomposition behavior.

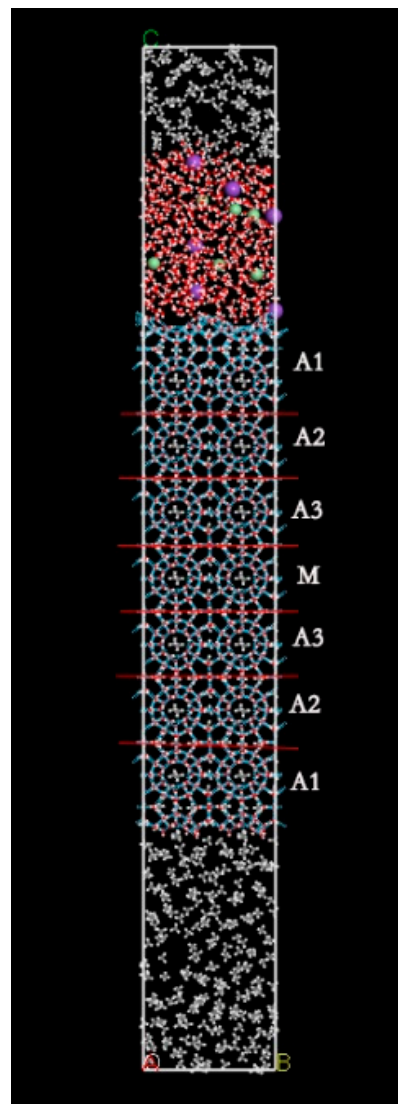


Figure 4. Layer division fashion for the hydrate system. Three layers near the liquid phase with the corresponding three layers near the gas phase (A1, A2, A3), and the middle layer (M).

The time required to complete dissociation for the corresponding layers (A1, A2, and A3) in the two side is used to describe the different dissociation behavior of hydrate slab in contact with liquid or gas phase, the details of the process as listed in Table 1.

Table 1. Required dissociation time (in picosecond) for each layer in different simulation temperature.

Temp.	243 K			247 K			253 K			263 K		
	L	G	T_{L-G}									
A1	370	860	−490	650	850	−200	230	715	−485	145	415	−270
A2	2200	890	+1310	985	455	+530	435	575	−140	280	340	−60
A3	930	910	+20	845	820	+25	735	520	+215	425	260	+165

T_{L-G} represent the time difference between liquid side and gas side. The −ve sign indicates the less dissociation time that is required for the liquid side when compared to the gas side, and the +ve sign means that the liquid side needed more time to dissociate completely.

From Table 1, it is evident that the liquid side takes less time for the dissociation of layer A1 when compared to the layer A2 and A3. The difference in dissociation time decreases gradually, and later the phenomena turn vice-versa as the required time in gas phase side reduces. It means that the liquid side has a faster dissociation rate at the beginning of the process, but as dissociation goes on the dissociation rate of gas side exceeds liquid side. The changes of T_{L-G} in different temperature clearly point out the dissociation rate and time variation between the two phases.

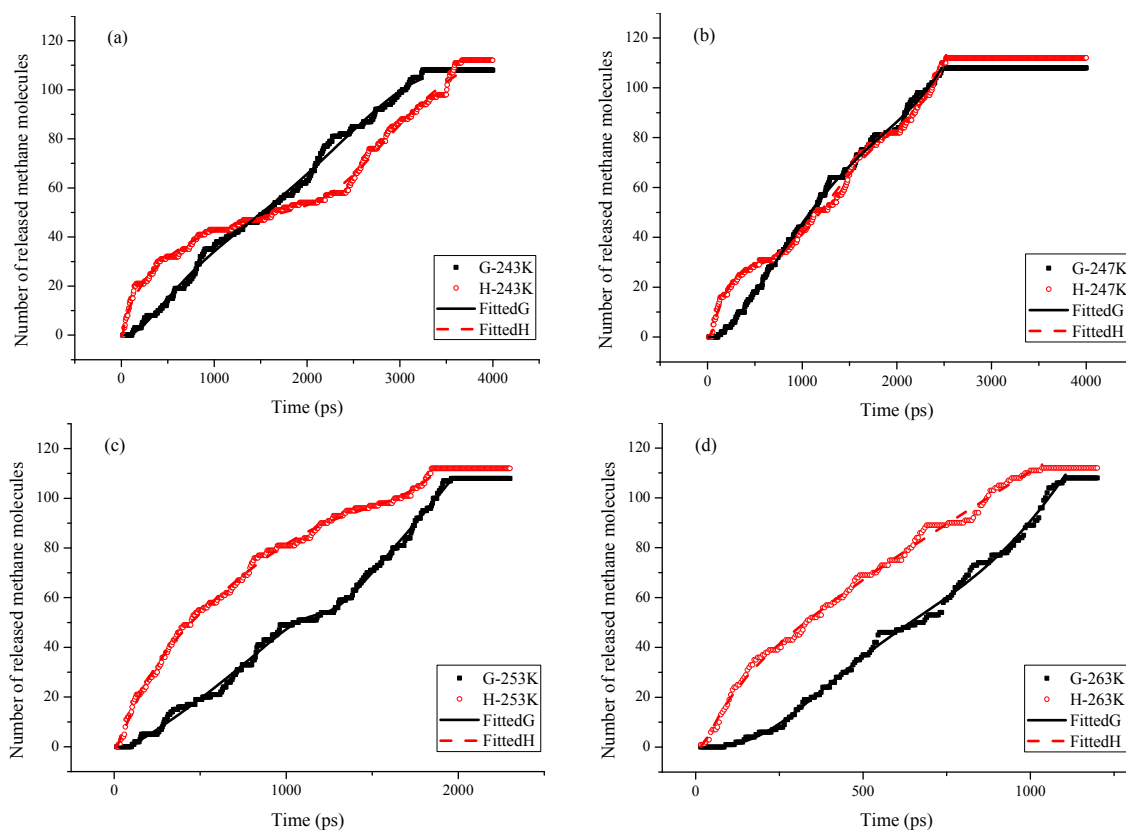


Figure 5. The number of CH_4 molecules released from liquid and gas side in various simulation temperature. (a) in 243 K, (b) in 247 K, (c) in 253 K, (d) in 263 K.

For more insight regarding the dissociation behavior of both phases, we showed the release rate of CH_4 molecules. Figure 5 demonstrates the number of CH_4 molecules that were released from liquid and gas side at different simulation temperature. There are 108 CH_4 molecules on the gas side and 112 CH_4 molecules on the liquid side (neglecting the total number of CH_4 molecules in the partial cages). Only CH_4 molecules that are in closed cages are counted to avoid the effect of quickly methane diffusion in partial cages. The established correlation relates to the number of released CH_4 molecules and the hydrate dissociation progress, the slope of these curves represents the release rate. When one curve reached the final plateau, the corresponding side of the hydrate slab dissociated completely. To get a clear observation of the dissociation rate, the Levenberg-Marquardt method is used to fit the growth part of these curves (Figure 5).

Figure 5 shows the obtained fitted curves as a line, the fitting formula, and the coefficient of determination (R^2) of each fitted curve are available in Appendix A. The R^2 of each fitted curve are all higher than 99.5%, which means that the fitted curves can explain the changes of original curves in the degree of more than 99.5%. Rate changes of CH_4 molecules that are released from liquid and gas side can be obtained from the derivative of fitted curves, as shown in Figure 6.

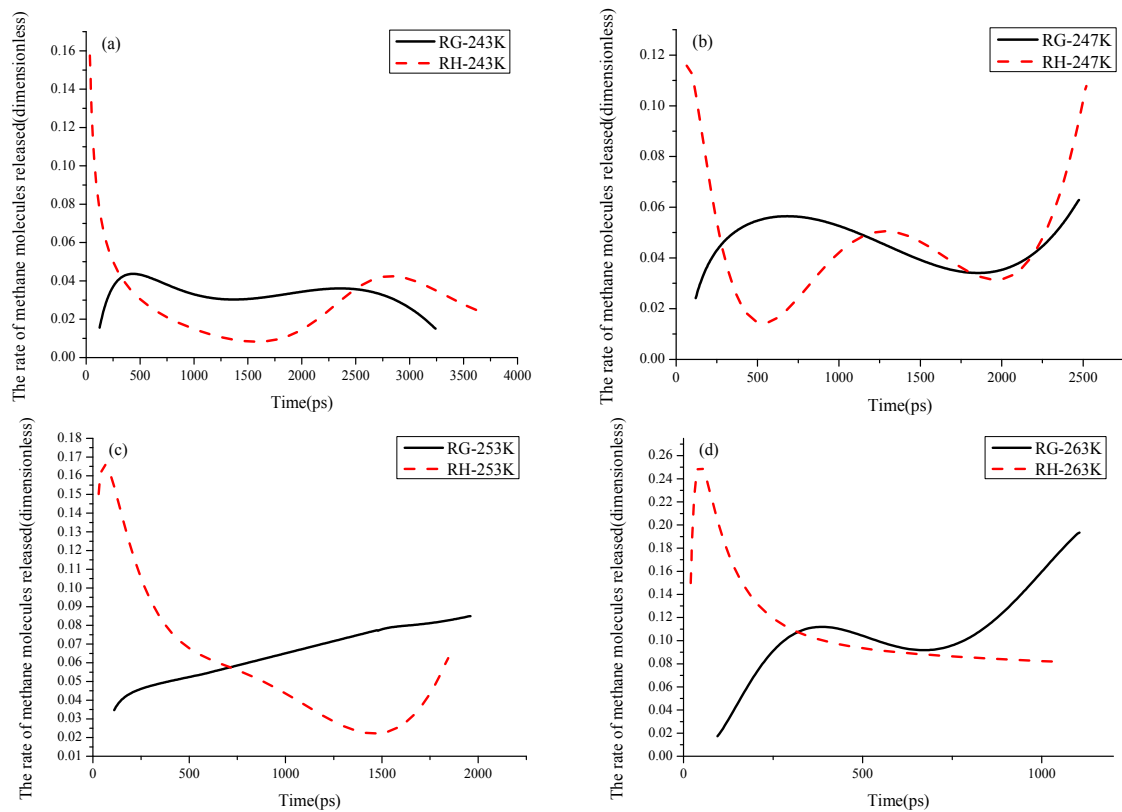


Figure 6. The rate changes of CH₄ molecules released from liquid and gas side in different simulation temperature. (a) in 243 K, (b) in 247 K, (c) in 253 K, (d) in 263 K.

In Figures 5 and 6 shows the CH₄ molecules in the liquid side having a higher release rate at the beginning of dissociation process, which means a faster rate of hydrate dissociation. The dissociation time for the liquid side started is also earlier than the gas side. However, the dissociation rate of the liquid side decreases quickly as the dissociation time prolongs.

Figure 6 demonstrates an apparent difference in the dissociation rate between the two phases. At higher temperatures of 253 K and 263 K, the dissociation rate of the liquid hydrate region may increase for over a short period at the beginning, when the temperature is lower, it will decrease first. Meanwhile, the dissociation rate of the gas side tends to increase or have a much less of a reduction effect. Due to these changes, the dissociation rate of gas side gradually surpasses the liquid side, and the higher dissociation rate makes the dissociation progress of gas side get close to the liquid side. At 243 K and 247 K, the gas side dissociation process even exceeds the liquid side, as seen in Figure 5. Then, a dynamic balance occurs between the dissociation rate of both sides. A reasonable explanation for this dissociation rate changes can be provided by the formation of liquid film outside the undecomposed hydrate layer.

The radial distribution functions (RDF) is used to describe the interaction from the inorganic salt ions to the hydrate structure. The mathematical expression of RDF is

$$g_{a-b}(r) = \frac{V}{N_a N_b} \left\langle \sum_{i=1}^{N_a} \frac{n_{ib}(r)}{4\pi r^2 \Delta r} \right\rangle \quad (1)$$

where N_a and N_b are the numbers of particle a and b , respectively; V is the volume of the simulation box; $n_{ib}(r)$ is the number of particle b within the distance of $r-r + \Delta r$ away from the i th particle a ; and, $g_{ab}(r)$ is the average probability of particle b appearing within the distance of $r-r + \Delta r$ away from the i th particle a .

At the beginning of dissociation process, the difference in hydrate dissociation rate is mainly caused by the gas and liquid fugacity difference. Higher fugacity of methane at the clathrate interface clearly decreases initial dissociation rates. The driving force of hydrate dissociation is higher at the hydrate-water interface and smaller at gas-hydrate interface. In addition, the electrostatic force from inorganic ions in liquid phase is also an impact to facilitate the dissociation rate in the liquid side. It attracts the water molecules in the hydrate system from escaping the restraint of hydrogen bonds. As seen in Figure 7, because of the opposite electric charges, the sodium and oxygen atom attract each other and generate a smaller distance than O–O. The negative charge on chloride induces the repulsion with oxygen atom, so the first peak locates at 3.2 Å, which is longer than both O–O and Na–O. It means that the sodium and chloride both have effect to water molecules in the crystalline structure of hydrate. Some of the water molecules attracted by the sodiums and some gain enough kinetic energy from the chloride to escape, thus can break down the water-cage structure of methane hydrate. These interaction phenomena facilitate the dissociation rate for hydrate layers. The simulation clearly shows the distinct difference in the preliminary dissociation rate between layers in touch with different phases. A liquid film is formed as dissociation continues, to cover the hydrate at the deep layer, thus hindering the transfer of mass, heat, and diffusion rate of methane molecules, reducing the rate of dissociation. The initial higher dissociation rate at the liquid side makes the film to appear earlier in the liquid side than the gas side. Thus, the film thickness is much greater on the liquid side when compared to the gas side at a given time. The liquid film also formed in gas side, however in a later period, and the dissociation process has decreased the fugacity of methane molecules near the hydrate-gas interface. Thus, smaller effect compared to the liquid side. At lower temperatures of 243 K and 247 K, the liquid film formed earlier than at higher temperatures because of the poor diffusion ability of water molecules, so the dissociation rate of the liquid side is decreased at the initial period. The longer time that is required for complete dissociation also gives enough time for the gas side to exceed the liquid side.

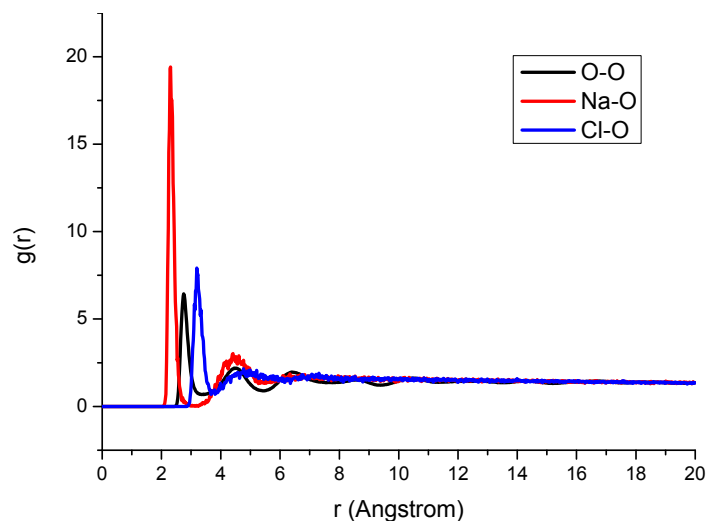


Figure 7. Radial distribution functions for Na^+ , Cl^- , and oxygen atom.

Earlier research [45] suggests that the diffusion of methane molecules is an important step, which influences the overall dissociation rate. The difference between methane molecules diffusion rate in different phases is also an important factor when studying the overall dissociation of hydrates. The diffusion of gas molecules in the liquid phase is more difficult than in the gas phase, about one order of magnitude. The mean square displacement (MSD) is used to describe the diffusion properties

of the CH₄ molecules in the two sides during the simulation process. The description of (MSD) is defined by the equation below.

$$MSD = R(t) = \frac{1}{N} \sum_{i=1}^N \langle |R_i(t) - R_i(t_0)|^2 \rangle \quad (2)$$

The “< >” brackets mean the average value $R_i(t) - R_i(t_0)$ is the displacement of particle i from time t_0 to t , and N is the total number of particles that are in the system.

The diffusion coefficients D can be calculated from the MSD curves, using the Einstein equation.

$$6Dt = R(t) \quad (3)$$

Figure 8 shows the mean square displacement and diffusion coefficients of CH₄ molecules between the two sides. It is evident from this figure that the MSD of methane molecules in the liquid side is much lower than the gas side, meaning a larger diffusion resistance. The large difference of diffusion coefficients between liquid and gas side also proves the diffusion of methane molecules in liquid side is more difficult. Therefore, the dissociation rate of layers on the liquid side is lowered, making it possible for the dissociation rate in gas side to overpass the liquid side.

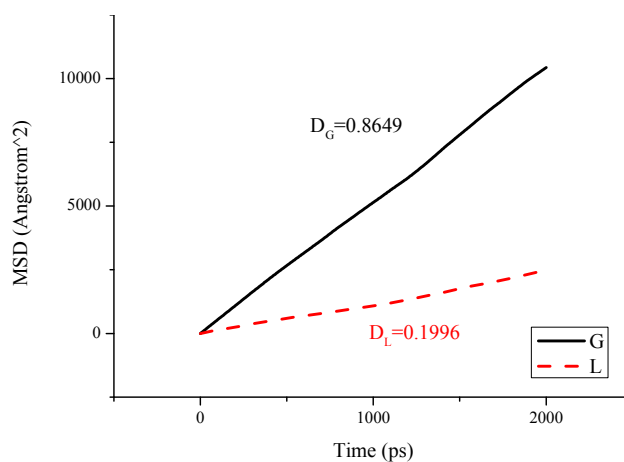


Figure 8. The mean square displacement of CH₄ molecules in the liquid and gas side.

Two factors lead to the dynamic balance in dissociation rate after the dissociation process in gas side exceeds the liquid side. First, is the formation of liquid film by which the gas side will gradually become larger than the liquid side due to the faster dissociation rate. The other factor is the formation of a methane nano-bubble, which will increase the dissociation rate [62]. The effect of nano-bubbles on the hydrate dissociation process had been fully studied by Yang et al. [63]. It can be found from the trajectory of simulation in 243 K that a nano-bubble formed in the liquid side after 2000 ps. Because of the higher diffusion of methane molecules in the gas side, the nano-bubble will be formed later with a smaller quantity. The resistance effect of liquid form, the formation of methane nano-bubbles, and the various methane diffusion in different phases together led to the dynamic balance of the two side as dissociation rate changes. This phenomenon needs further detailed analysis.

4. Conclusions

We used molecular dynamics simulation to study the dissociation behavior of methane hydrates in contact with methane gas and liquid water, 3.5% NaCl ions are added into the liquid phase to reproduce the seawater environment.

There are two main stages in the dissociation process, the fast diffusion of methane molecules in partial cages and the layer by layer breakdown of closed cages from the two interfaces towards the

center. The study shows that regardless of what phases the hydrate region is in contact in the seawater environment; the sedimentary dissociated trend moves from the outside interface to the core.

We also studied the difference in dissociation behavior for regions of hydrate-bearing sediments that are in contact with different phases in the seawater environment on the hydrate dissociation process. From the trajectory and methane release rate, the hydrate regions that are in contact with liquid phase show a faster-dissociated rate at the beginning of hydrate dissociation. As the dissociation continues, dissociation rate of hydrate regions in contact with liquid phase is gradually exceeded by the regions in contact with the gas phase due to the formation of liquid film and the difficulty of methane diffusion. The dissociation progress of hydrate layers in the gas side gradually catches up with the liquid side and it is easier to exceed the liquid side at lower temperatures. Our research was beneficial to perfect the microscopic mechanism of hydrate dissociation behavior in marine sediments, which was helpful in guiding the exploitation of methane hydrate in deep ocean regions.

Acknowledgments: This study was jointly supported by the National Natural Science Foundation of China (Grant No. 51404291 & NO. 51774317) and Evaluation and Detection Technology Laboratory of marine mineral resources, Qingdao National Laboratory for Marine Science and Technology (Grant No. KC201702). We are grateful to all staff involved in this project, and also wish to thank the journal editors and the reviewers whose constructive comments improved the quality of this paper greatly.

Author Contributions: Zhixue Sun, Haoxuan Wang, Ying Xin and Xuchen Zhu conceived and designed the experiments; Zhixue Sun and Haoxuan Wang created the simulation model; Jun Yao and Jianlong Kou contributed in idea generation, and provided several simulation methods; Zhixue Sun and Haoxuan Wang analyzed the result; Jun Yao contributed analysis tools; Haoxuan Wang wrote the manuscript; Weina Li, Chengwei Yang and Kelvin Bongole make a great contribution to the revision of manuscript.

Conflicts of Interest: The authors declare no conflict of interest.

Appendix A

The Levenberg-Marquardt method is used to fit the growth part of curves in Figure 6. The fitting formula and coefficient of determination (R^2) of each fitted curve are shown as follow.

1. G-243K:

Fitting formula

$$\begin{aligned}
 y &= p_1 + p_2x^{0.5} + p_3x + p_4x^{1.5} + p_5x^2 + p_6x^{2.5} + p_7x^3 \\
 p_1 &= -2.52289726384994 \\
 p_2 &= 1.98715014799801 \\
 p_3 &= -0.394304118899512 \\
 p_4 &= 0.0316769072017772 \\
 p_5 &= -0.00104681476978435 \\
 p_6 &= 1.59686078934991 \times 10^{-5} \\
 p_7 &= -9.18281641452352 \times 10^{-8} \\
 R^2 &= 0.9962
 \end{aligned}$$

Coefficient of determination $R^2 = 0.9962$

2. H-243K:

Fitting formula

$$y = \frac{(p_1 + p_3x^{0.5} + p_5x + p_7x^{1.5} + p_9x^2 + p_{11}x^{2.5})}{(1 + p_2x^{0.5} + p_4x + p_6x^{1.5} + p_8x^2 + p_{10}x^{2.5})}$$

$$p_1 = 0.0264367199337785$$

$$p_2 = -41716.3312935935$$

$$p_3 = 274685.187663359$$

$$p_4 = 14554.6908637279$$

$$p_5 = -179555.204487187$$

$$p_6 = -438.600302369739$$

$$p_7 = 32608.0637423048$$

$$p_8 = 2.55447092191608$$

$$p_9 = -1074.68231254855$$

$$p_{10} = 0.0203536259504544$$

$$p_{11} = 10.2199063904669$$

Coefficient of determination $R^2 = 0.9950$

3. G-247K

Fitting formula

$$y = p_1 + p_2x^{0.5} + p_3x + p_4x^{1.5} + p_5x^2 + p_6x^{2.5} + p_7x^3 + p_8x^{3.5}$$

$$p_1 = -0.158989402741885$$

$$p_2 = 0.542274716063813$$

$$p_3 = -0.189281702116761$$

$$p_4 = 0.021725279441181$$

$$p_5 = -0.00102603941277418$$

$$p_6 = 2.93891864685635 \times 10^{-5}$$

$$p_7 = -4.70401159229296 \times 10^{-7}$$

$$p_8 = 3.09616247066469 \times 10^{-9}$$

Coefficient of determination $R^2 = 0.9981$

4. H-247K

Fitting formula

$$y = p_1 + p_2x^{0.5} + p_3x + p_4x^{1.5} + p_5x^2 + p_6x^{2.5} + p_7x^3 + p_8x^{3.5}$$

$$p_1 = -1.1622210978288$$

$$p_2 = 0.822868898441985$$

$$p_3 = -0.368394466952489$$

$$p_4 = 0.0825999711751837$$

$$p_5 = -0.00616104356405071$$

$$p_6 = 0.000210230039224945$$

$$p_7 = -3.36262963259856 \times 10^{-6}$$

$$p_8 = 2.05027640511381 \times 10^{-8}$$

Coefficient of determination $R^2 = 0.9974$

5. G-253K

Fitting formula

$$y = \frac{(p_1 + p_3x + p_5x^2 + p_7x^3 + p_9x^4 + p_{11}x^5 + p_{13}x^6)}{(1 + p_2x + p_4x^2 + p_6x^3 + p_8x^4 + p_{10}x^5 + p_{12}x^6)}$$

$$p_1 = -0.104657402631542$$

$$p_2 = -76.6034589415333$$

$$p_3 = -1826.57412403309$$

$$p_4 = 43.9898122348601$$

$$p_5 = 442.011907991095$$

$$p_6 = 3.52693215036982$$

$$p_7 = -18.414094583349$$

$$p_8 = -0.00624425222888123$$

$$p_9 = 0.193728968273972$$

$$p_{10} = 3.19074273510536 \times 10^{-6}$$

$$p_{11} = -0.000274547672040276$$

$$p_{12} = -3.27945386591798 \times 10^{-10}$$

$$p_{13} = 1.07745139185719 \times 10^{-7}$$

Coefficient of determination $R^2 = 0.9968$

6. H-253K

Fitting formula

$$y = p_1 + p_2x^{0.5} + p_3x + p_4x^{1.5} + p_5x^2 + p_6x^{2.5} + p_7x^3 + p_8x^{3.5}$$

$$p_1 = -0.347494418118165$$

$$p_2 = -0.299606826446903$$

$$p_3 = -0.0232237136440884$$

$$p_4 = 0.0491603748781263$$

$$p_5 = -0.00441657774258649$$

$$p_6 = 0.000171380285065007$$

$$p_7 = -3.14844063545478 \times 10^{-6}$$

$$p_8 = 2.2310472020647 \times 10^{-8}$$

Coefficient of determination $R^2 = 0.9978$

7. G-263K

Fitting formula

$$y = p_1 + p_2x^{0.5} + p_3x + p_4x^{1.5} + p_5x^2 + p_6x^{2.5} + p_7x^3 + p_8x^{3.5} + p_9x^4$$

$$p_1 = -0.0047046349507421$$

$$p_2 = -0.248721182471245$$

$$p_3 = -0.000148461268640836$$

$$p_4 = 0.0348788371306938$$

$$p_5 = -0.00808072453075961$$

$$p_6 = 0.000768606886412719$$

$$p_7 = -3.41356235135758 \times 10^{-5}$$

$$p_8 = 7.15466922733688 \times 10^{-7}$$

$$p_9 = -5.71844706478173 \times 10^{-9}$$

Coefficient of determination $R^2 = 0.9970$

8. H-263K

Fitting formula

$$y = \sqrt{\frac{p_1 + p_3x + p_5x^2}{1 + p_2x + p_4x^2}}$$

$$p_1 = -1.611542751$$

$$p_2 = 0.021348885$$

$$p_3 = 0.139626369$$

$$p_4 = 5.50 \times 10^{-6}$$

$$p_5 = 0.000154835$$

Coefficient of determination $R^2 = 0.9966$

References

- Sloan, E.D. Fundamental principles and applications of natural gas hydrates. *Nature* **2003**, *426*, 353–363. [[CrossRef](#)] [[PubMed](#)]
- Kvenvolden, K.A. Gas hydrate and humans. *Ann. N. Y. Acad. Sci.* **2000**, *912*, 17–22. [[CrossRef](#)]
- Yang, Y.; He, Y.; Zheng, Q. An analysis of the key safety technologies for natural gas hydrate exploitation. *Adv. Geo-Energy Res.* **2017**, *1*, 100–104. [[CrossRef](#)]
- Kida, M.; Suzuki, K.; Kawamura, T.; Oyama, H.; Nagao, J.; Ebinuma, T.; Narita, H. Characteristics of natural gas hydrates occurring in pore-spaces of marine sediments collected from the eastern Nankai Trough, off Japan. *Energy Fuels* **2009**, *23*, 5580–5586. [[CrossRef](#)]
- Shimada, W.; Takeya, S.; Kamata, Y.; Uchida, T.; Nagao, J.; Ebinuma, T.; Narita, H. Texture change of ice on anomalously preserved methane clathrate hydrate. *J. Phys. Chem. B* **2005**, *109*, 5802–5807. [[CrossRef](#)] [[PubMed](#)]
- Misyura, S.Y. The influence of porosity and structural parameters on different kinds of gas hydrate dissociation. *Sci. Rep.* **2016**, *6*, 30324. [[CrossRef](#)] [[PubMed](#)]
- Misyura, S.Y.; Donskoy, I.G. Dissociation of natural and artificial gas hydrate. *Chem. Eng. Sci.* **2016**, *148*, 65–77. [[CrossRef](#)]
- Takeya, S.; Ebinuma, T.; Uchida, T.; Nagao, J.; Narita, H. Self-preservation effect and dissociation rates of CH₄ hydrate. *J. Cryst. Growth* **2002**, *237*, 379–382. [[CrossRef](#)]
- Konno, Y.; Jin, Y.; Shinjou, K.; Nagao, J. Experimental evaluation of the gas recovery factor of methane hydrate in sandy sediment. *RSC Adv.* **2014**, *4*, 51666–51675. [[CrossRef](#)]
- Clarke, M.A.; Bishnoi, P.R. Determination of the intrinsic rate constant and activation energy of CO₂ gas hydrate decomposition using in-situ particle size analysis. *Chem. Eng. Sci.* **2004**, *59*, 2983–2993. [[CrossRef](#)]
- Kneafsey, T.J.; Tomutsa, L.; Moridis, G.J.; Seol, Y.; Freifeld, B.M.; Taylor, C.E.; Gupta, A. Methane hydrate formation and dissociation in a partially saturated core-scale sand sample. *J. Pet. Sci. Eng.* **2007**, *56*, 108–126. [[CrossRef](#)]
- Kakati, H.; Kar, S.; Mandal, A. Methane hydrate formation and dissociation in oil-in-water emulsion. *Energy Fuels* **2014**, *28*, 4440–4446. [[CrossRef](#)]
- Link, D.D.; Ladner, E.P.; Elsen, H.A.; Taylor, C.E. Formation and dissociation studies for optimizing the uptake of methane by methane hydrates. *Fluid Phase Equilib.* **2003**, *211*, 1–10. [[CrossRef](#)]
- Gupta, A.; Moridis, G.J.; Kneafsey, T.J.; Sloan, E.D. Modeling pure methane hydrate dissociation using a numerical simulator from a novel combination of X-ray computed tomography and macroscopic data. *Energy Fuels* **2009**, *23*, 5958–5965. [[CrossRef](#)]
- Moridis, G.J.; Kowalsky, M.B.; Pruess, K. Depressurization-induced gas production from class-1 hydrate deposits. *SPE Reserv. Eval. Eng.* **2007**, *10*, 458–481. [[CrossRef](#)]
- Konno, Y.; Masuda, Y.; Akamine, K.; Naiki, M.; Nagao, J. Sustainable gas production from methane hydrate reservoirs by the cyclic depressurization method. *Energy Convers. Manag.* **2016**, *108*, 439–445. [[CrossRef](#)]
- Luis, D.P.; García-González, A.; Saint-Martin, H. A Theoretical Study of the Hydration of Methane, from the Aqueous Solution to the sI Hydrate-Liquid Water-Gas Coexistence. *Int. J. Mol. Sci.* **2016**, *17*, 378. [[CrossRef](#)] [[PubMed](#)]

18. Sun, Z.; Xin, Y.; Sun, Q.; Ma, R.; Zhang, J.; Lv, S.; Cai, M.; Wang, H. Numerical Simulation of the Depressurization Process of a Natural Gas Hydrate Reservoir: An Attempt at Optimization of Field Operational Factors with Multiple Wells in a Real 3D Geological Model. *Energies* **2016**, *9*, 714. [[CrossRef](#)]
19. Miyoshi, T.; Ohmura, R.; Yasuoka, K. Predicting thermodynamic stability of clathrate hydrates based on molecular-dynamics simulations and its confirmation by phase-equilibrium measurements. *J. Phys. Chem. C* **2007**, *111*, 3799–3802. [[CrossRef](#)]
20. Hakim, L.; Koga, K.; Tanaka, H. Phase behavior of different forms of ice filled with hydrogen molecules. *Phys. Rev. Lett.* **2010**, *104*, 115701. [[CrossRef](#)] [[PubMed](#)]
21. Hakim, L.; Koga, K.; Tanaka, H. Thermodynamic stability of hydrogen hydrates of ice I_c and II structures. *Phys. Rev. B* **2010**, *82*, 144105. [[CrossRef](#)]
22. Michalis, V.K.; Costandy, J.; Tsimpanogiannis, I.N. Prediction of the phase equilibria of methane hydrates using the direct phase coexistence methodology. *J. Chem. Phys.* **2015**, *142*, 044501. [[CrossRef](#)] [[PubMed](#)]
23. Conde, M.; Vega, C.; McBride, C.; Noya, E.G.; Ramírez, R.; Sesé, L.M. Can gas hydrate structures be described using classical simulations? *J. Chem. Phys.* **2010**, *132*, 114503. [[CrossRef](#)] [[PubMed](#)]
24. English, N.J.; John, S.T. Pressure-induced amorphization of methane hydrate. *Phys. Rev. B* **2012**, *86*, 104109. [[CrossRef](#)]
25. Nath, C.S.; Gelb, L.D. A Monte Carlo simulation study of methane clathrate hydrates confined in slit-shaped pores. *J. Phys. Chem. B* **2012**, *116*, 2183–2197. [[CrossRef](#)] [[PubMed](#)]
26. English, N.J.; Tse, J.S. Perspectives on hydrate thermal conductivity. *Energies* **2010**, *3*, 1934–1942. [[CrossRef](#)]
27. Krivchikov, A.I.; Korolyuk, O.A.; Romantsova, O. Heat transfer in crystalline clathrate hydrates at low temperatures. *Low Temp. Phys.* **2007**, *33*, 798–804. [[CrossRef](#)]
28. Jiang, H.; Jordan, K.D. Comparison of the Properties of Xenon, Methane, and Carbon Dioxide Hydrates from Equilibrium and Nonequilibrium Molecular Dynamics Simulations. *J. Phys. Chem. C* **2009**, *114*, 5555–5564. [[CrossRef](#)]
29. English, N.J.; Gorman, P.D.; MacElroy, J.M.D. Mechanisms for thermal conduction in hydrogen hydrate. *J. Chem. Phys.* **2012**, *136*, 044501. [[CrossRef](#)] [[PubMed](#)]
30. Jacobson, L.C.; Hujo, W.; Molinero, V. Amorphous precursors in the nucleation of clathrate hydrates. *J. Am. Chem. Soc.* **2010**, *132*, 11806–11811. [[CrossRef](#)] [[PubMed](#)]
31. Walsh, M.R.; Koh, C.A.; Sloan, E.D.; Sum, A.K.; Wu, D.T. Microsecond simulations of spontaneous methane hydrate nucleation and growth. *Science* **2009**, *326*, 1095–1098. [[CrossRef](#)] [[PubMed](#)]
32. Walsh, M.R.; Rainey, J.D.; Lafond, P.G. The cages, dynamics, and structuring of incipient methane clathrate hydrates. *Phys. Chem. Chem. Phys.* **2011**, *13*, 19951–19959. [[CrossRef](#)] [[PubMed](#)]
33. Walsh, M.R.; Beckham, G.T.; Koh, C.A.; Sloan, E.D.; Wu, D.T.; Sum, A.K. Methane hydrate nucleation rates from molecular dynamics simulations: Effects of aqueous methane concentration, interfacial curvature, and system size. *J. Phys. Chem. C* **2011**, *115*, 21241–21248. [[CrossRef](#)]
34. Sarupria, S.; Debenedetti, P.G. Homogeneous nucleation of methane hydrate in microsecond molecular dynamics simulations. *J. Phys. Chem. Lett.* **2012**, *3*, 2942–2947. [[CrossRef](#)] [[PubMed](#)]
35. Tung, Y.T.; Chen, L.J.; Chen, Y.P.; Lin, S.T. The growth of structure I methane hydrate from molecular dynamics simulations. *J. Phys. Chem. B* **2010**, *114*, 10804–10813. [[CrossRef](#)] [[PubMed](#)]
36. Tung, Y.T.; Chen, L.J.; Chen, Y.P.; Lin, S.T. Growth of structure I carbon dioxide hydrate from molecular dynamics simulations. *J. Phys. Chem. C* **2011**, *115*, 7504–7515. [[CrossRef](#)]
37. Liang, S.; Kusalik, P.G. Explorations of gas hydrate crystal growth by molecular simulations. *Chem. Phys. Lett.* **2010**, *494*, 123–133. [[CrossRef](#)]
38. Vatamanu, J.; Kusalik, P.G. Molecular insights into the heterogeneous crystal growth of sI methane hydrate. *J. Phys. Chem. B* **2006**, *110*, 15896–15904. [[CrossRef](#)] [[PubMed](#)]
39. Vatamanu, J.; Kusalik, P.G. Heterogeneous crystal growth of methane hydrate on its sII crystallographic face. *J. Phys. Chem. B* **2008**, *112*, 2399–2404. [[CrossRef](#)] [[PubMed](#)]
40. Báez, L.A.; Clancy, P. Computer simulation of the crystal growth and dissolution of natural gas hydrates. *Ann. N. Y. Acad. Sci.* **1994**, *715*, 177–186. [[CrossRef](#)]
41. Tse, J.S.; Klug, D.D. Formation and decomposition mechanisms for clathrate hydrates. *J. Supramol. Chem.* **2002**, *2*, 467–472. [[CrossRef](#)]

42. Takeya, S.; Yoneyama, A.; Ueda, K.; Hyodo, K.; Takeda, T.; Mimachi, H.; Gotoh, Y. Nondestructive imaging of anomalously preserved methane clathrate hydrate by phase contrast X-ray imaging. *J. Phys. Chem. C* **2011**, *115*, 16193–16199. [[CrossRef](#)]
43. Takeya, S.; Ripmeester, J.A. Anomalous preservation of CH₄ hydrate and its dependence on the morphology of hexagonal ice. *ChemPhysChem* **2010**, *11*, 70–73. [[CrossRef](#)] [[PubMed](#)]
44. English, N.J.; MacElroy, J.M.D. Theoretical studies of the kinetics of methane hydrate crystallization in external electromagnetic fields. *J. Chem. Phys.* **2004**, *120*, 10247–10256. [[CrossRef](#)] [[PubMed](#)]
45. English, N.J.; Phelan, G.M. Molecular dynamics study of thermal-driven methane hydrate dissociation. *J. Chem. Phys.* **2009**, *131*, 074704. [[CrossRef](#)] [[PubMed](#)]
46. English, N.J.; Clarke, E.T. Molecular dynamics study of CO₂ hydrate dissociation: Fluctuation-dissipation and non-equilibrium analysis. *J. Chem. Phys.* **2013**, *139*, 094701. [[CrossRef](#)] [[PubMed](#)]
47. Myshakin, E.M.; Jiang, H.; Warzinski, R.P.; Jordan, K.D. Molecular dynamics simulations of methane hydrate decomposition. *J. Phys. Chem. A* **2009**, *113*, 1913–1921. [[CrossRef](#)] [[PubMed](#)]
48. Bagherzadeh, S.A.; Englezos, P.; Alavi, S.; Ripmeester, J.A. Molecular modeling of the dissociation of methane hydrate in contact with a silica surface. *J. Phys. Chem. B* **2012**, *116*, 3188–3197. [[CrossRef](#)] [[PubMed](#)]
49. Alavi, S.; Ripmeester, J.A. Nonequilibrium adiabatic molecular dynamics simulations of methane clathrate hydrate decomposition. *J. Chem. Phys.* **2010**, *132*, 144703. [[CrossRef](#)] [[PubMed](#)]
50. Bagherzadeh, S.A.; Englezos, P.; Alavi, S.; Ripmeester, J.A. Molecular simulation of non-equilibrium methane hydrate decomposition process. *J. Chem. Thermodyn.* **2012**, *44*, 13–19. [[CrossRef](#)]
51. Mimachi, H.; Takeya, S.; Gotoh, Y.; Yoneyama, A.; Hyodo, K.; Takeda, T.; Murayama, T. Dissociation behaviors of methane hydrate formed from NaCl solutions. *Fluid Phase Equilib.* **2016**, *413*, 22–27. [[CrossRef](#)]
52. Xu, J.; Gu, T.; Sun, Z.; Li, X.; Wang, X. Molecular dynamics study on the dissociation of methane hydrate via inorganic salts. *Mol. Phys.* **2016**, *114*, 34–43. [[CrossRef](#)]
53. Gutt, C.; Asmussen, B.; Press, W. The structure of deuterated methane-hydrate. *J. Chem. Phys.* **2000**, *113*, 4713–4721. [[CrossRef](#)]
54. Greathouse, J.A.; Cygan, R.T.; Simmons, B.A. Vibrational spectra of methane clathrate hydrates from molecular dynamics simulation. *J. Phys. Chem. B* **2006**, *110*, 6428–6431. [[CrossRef](#)] [[PubMed](#)]
55. Geng, C.Y.; Wen, H.; Zhou, H. Molecular simulation of the potential of methane reoccupation during the replacement of methane hydrate by CO₂. *J. Phys. Chem. A* **2009**, *113*, 5463–5469. [[CrossRef](#)] [[PubMed](#)]
56. Geng, C.Y.; Han, Q.Z.; Wen, H.; Dai, Z.; Song, C. Molecular dynamics simulation on the decomposition of type SII hydrogen hydrate and the performance of tetrahydrofuran as a stabiliser. *Mol. Simul.* **2010**, *36*, 474–483. [[CrossRef](#)]
57. Liu, Y.; Zhao, J.; Xu, J. Dissociation mechanism of carbon dioxide hydrate by molecular dynamic simulation and ab initio calculation. *Comput. Theor. Chem.* **2012**, *991*, 165–173. [[CrossRef](#)]
58. Burnham, C.J.; English, N.J. Study of clathrate hydrates via equilibrium molecular-dynamics simulation employing polarisable and non-polarisable, rigid and flexible water models. *J. Chem. Phys.* **2016**, *144*, 164503. [[CrossRef](#)] [[PubMed](#)]
59. Conde, M.M.; Vega, C. A simple correlation to locate the three phase coexistence line in methane-hydrate simulations. *J. Chem. Phys.* **2013**, *138*, 056101. [[CrossRef](#)] [[PubMed](#)]
60. Míguez, J.M.; Conde, M.M.; Torrè, J.P.; Blas, F.J.; Piñeiro, M.M.; Vega, C. Molecular dynamics simulation of CO₂ hydrates: Prediction of three phase coexistence line. *J. Chem. Phys.* **2015**, *142*, 124505. [[CrossRef](#)] [[PubMed](#)]
61. Marshall, D.R.; Saito, S.; Kobayashi, R. Hydrates at high pressures: Part I. Methane-water, argon-water, and nitrogen-water systems. *AIChE J.* **1964**, *10*, 202–205. [[CrossRef](#)]
62. Yagasaki, T.; Matsumoto, M.; Andoh, Y.; Okazaki, S. Effect of bubble formation on the dissociation of methane hydrate in water: A molecular dynamics study. *J. Phys. Chem. B* **2014**, *118*, 1900–1906. [[CrossRef](#)] [[PubMed](#)]
63. Yang, L.; Falenty, A.; Chaouachi, M.; Habertür, D.; Kuhs, W.F. Synchrotron X-ray computed microtomography study on gas hydrate decomposition in a sedimentary matrix. *Geochem. Geophys. Geosyst.* **2016**, *17*, 3717–3732. [[CrossRef](#)]

